International Journal of Extreme Manufacturing

PAPER • OPEN ACCESS

Laser additive manufacturing of high-resolution microscale shell lattices by toolpath engineering

To cite this article: Junhao Ding *et al* 2026 *Int. J. Extrem. Manuf.* **8** 015002

View the article online for updates and enhancements.

You may also like

- Insights into biodegradable Mn-incorporated Fe-based scaffolds in orthopedics: bridging manufacturing techniques, physicomechanical properties, and multifunctional bioapplications
Xin Huang, Ming-Chun Zhao, Qi Yin et al.
- Advanced biofabrication techniques of muscle cell-powered biohybrid robots
Niyou Wang, Yipei Yang, Zahra Rezaei et al.
- Fiber composites-based flexible triboelectric nanogenerators: from material design to emerging applications
Gang Yu, Han Hu, Qianguo Yu et al.

This content was downloaded from IP address 158.132.161.180 on 27/01/2026 at 04:13

OPEN ACCESS
IMMT | IOP Publishing
International Journal of Extreme Manufacturing
Int. J. Extrem. Manuf. **8** (2026) 015002 (15pp)
https://doi.org/10.1088/2631-7990/ae01ff

Laser additive manufacturing of high-resolution microscale shell lattices by toolpath engineering

Junhao Ding[1], Shuo Qu[1], Shengbiao Zhang[2], Zongxin Hu[1], Zhenyong Feng[3], Tianyu Gao[4], Ming Wang Fu[3,*], Lei Zhang[5,6], Chinnapat Panwisawas[7], Wen Chen[2,*] and Xu Song[1,*]

[1] Department of Mechanical and Automation Engineering, Chinese University of Hong Kong, Hong Kong Special Administrative Region of China, People's Republic of China
[2] Department of Mechanical and Industrial Engineering, University of Massachusetts, Amherst, MA 01003, United States of America
[3] Department of Mechanical Engineering, The Hong Kong Polytechnic University, Hung Hom, Kowloon, Hong Kong Special Administrative Region of China, People's Republic of China
[4] School of Traffic & Transportation Engineering, Central South University, Changsha, Hunan 410083, People's Republic of China
[5] Meta Robot Institute, Shanghai Jiao Tong University, Shanghai 200240, People's Republic of China
[6] State Key Laboratory of Mechanical System and Vibration, Shanghai Jiao Tong University, Shanghai 200240, People's Republic of China
[7] School of Engineering and Materials Science, Queen Mary University of London, London E1 4NS, United Kingdom

E-mail: mmmwfu@polyu.edu.hk, wenchen@umass.edu and xsong@mae.cuhk.edu.hk

Received 24 February 2025, revised 4 May 2025
Accepted for publication 2 September 2025
Published 29 September 2025

Abstract

Laser additively manufactured microscale metallic lattices show great potential for high-performance applications, yet trade-offs among geometric precision, structural integrity, and computational efficiency still persist. Here, we introduce a stereolithography file format-free (STL-free) hybrid toolpath generation method for laser-based powder bed fusion (PBF-LB) that synergizes implicit geometric modeling with optimized laser scanning strategy, overcoming these limitations. By circumventing traditional mesh-based workflows, our method directly translates implicit lattice geometries into laser toolpaths while precisely regulating energy deposition trajectories. This mesh-free process enables the fabrication of complex shell lattices with ultra-thin walls and enhanced surface quality. In addition to reducing memory usage and processing time by up to 90%, the method yields a synergistic enhancement in mechanical performance, notably improving both strength and toughness. By bridging computational design and fabrication, this framework enables the scalable production of high-performance microscale lattices and unlocks their potential for industrial applications.

* Authors to whom any correspondence should be addressed.

Original content from this work may be used under the terms of the Creative Commons Attribution 4.0 licence. Any further distribution of this work must maintain attribution to the author(s) and the title of the work, journal citation and DOI.

© 2025 The Author(s). Published by IOP Publishing Ltd on behalf of the IMMT

Supplementary material for this article is available online

Keywords: toolpath engineering, STL-free hybrid toolpath, high-resolution printing, laser-based powder bed fusion, microscale lattices

1. Introduction

Metamaterials, a class of engineered structures, are known for their exceptional properties that are unattainable in bulk materials[1–3]. By precisely manipulating design parameters, they can achieve unique functionalities such as multistability[4,5], tunable stiffness[6,7], bio-compatibility[8], and energy absorption[9,10]. Among them, metallic shell-based metamaterials, particularly at microscale, have shown great potential for application in industries like aerospace[11], biomedical[12], and automotive[13], where extreme mechanical performance and miniaturization are simultaneously required.

Laser-based powder bed fusion (PBF-LB), a dominant technology in metal additive manufacturing, has played a pivotal role in the fabrication of metallic lattice structures[14–16]. However, achieving the necessary resolution and precision at microscale while maintaining structural integrity remains a significant challenge[17,18]. Conventional PBF-LB systems, typically operating with scan track widths between 150 μm and 300 μm, struggle to fabricate fine structural features such as thin shells and high-curvature surfaces[19], which are critical for applications like bone scaffolds and dental implants[8,20,21]. Most existing lattice designs employ unit cell sizes ranging from 3 mm to 10 mm and suffer from significant surface roughness (Ra: 15–30 μm, with powder particle size D_{50} around 30 μm)[14,22,23], rendering them unsuitable for those applications[24,25]. To address these limitations, laser scanning strategies such as Zig-Zag[26], rotation 67° (R67)[27], and AI-enabled toolpaths[28] have been developed for interior filling, while contour scanning enhances surface quality. Yet, further reduction in feature size demands more specialized toolpath planning.

The fabrication of thin-walled lattice structures is fundamentally constrained by the laser beam spot size and the stability of molten pool dynamics during single-track scanning. The walls thinner than 100 μm face process instabilities such as powder recoating, spattering, and balling defects[29,30]. For example, grid-like thin-wall structures, fabricated using single-track strategies, often exhibit surface defects (e.g., adhered particles, burrs, and discontinuities) with surface roughness values around $Ra = 11$ μm, alongside pores and microcracks[31]. Experimental and computational studies of molten pool behavior in multilayer tungsten tracks have demonstrated that low energy densities, required for thinner walls, exacerbate balling and track discontinuity[32].

Shell-based lattices, particularly triply periodic minimal surfaces (TPMS), further complicate the manufacturing situation due to extensive overhangs and curved surfaces[33]. Common defects in such structures include thickness variation, through-thickness porosity, surface waviness, and roughness[34]. For instance, when fabricating Schwarz-Primitive shell lattices in Ti6Al4V via single-track contour scanning, through-hole defects were observed in overhang regions[34,35]. These persistent challenges underscore the urgent need for advanced fabrication strategies that enable finer feature control, especially in overhang-dominated geometries.

In parallel, the computational pipeline for generating high-resolution lattice structures remains inefficient. Traditional workflows rely heavily on STL files, which tessellate implicit geometries into surface meshes for slicing and toolpath generation[36]. This conversion degrades geometric fidelity, particularly in smoothly curved thin shells, and imposes a significant computational burden[37,38]. For complex shell lattices, the trade-off between mesh resolution and processing time becomes a major bottleneck[39,40]. While improvements in STL meshing and slicing have been proposed, they remain limited to relatively simple geometries and do not scale well to intricate topologies[40]. Recent studies suggest that direct slicing of implicit representations[41–43], could bypass these limitations, offering significant efficiency gains and unlocking new potential for fabricating TPMS lattices.

Here, we present an STL-free hybrid toolpath planning strategy specifically developed for an open-source PBF-LB system to fabricate complex shell lattice structures. This approach directly converts implicit lattice geometries into laser scanning paths, entirely bypassing the STL conversion process. As a result, computational memory usage and processing time are reduced by up to 90%. The hybrid toolpath strategy enables the fabrication of ultra-thin walls with thicknesses as low as 65 μm through single-track scanning, while maintaining structural integrity in overhang regions via an adaptive R67 path. The precisely controlled laser scanning path ensures a stabilized energy input density, leading to high surface quality with a surface roughness as low as $Ra = 3.2$ μm. This methodology significantly enhances computational efficiency, geometric fidelity, and printing quality. Notably, the proposed strategy is versatile and readily adaptable to other powder bed fusion platforms, paving the way for high-precision manufacturing in applications such as mechanical energy absorbers, heat exchangers, and biomedical implants.

2. Method

2.1. PBF-LB fabrication

An in-house developed PBF-LB system, Hans M100μ, was employed for the experimental work. The system is equipped with a fiber laser operating at a wavelength of 1 070 nm, with

a beam spot size of 25 μm. To maintain optimal atmospheric conditions during processing, the build chamber was purged with nitrogen gas, ensuring an oxygen concentration below 0.05%. Gas-atomized spherical 316L stainless steel powder, with particle diameters ranging from 5 μm to 25 μm (median diameter, D_{50} = 16.3 μm), was sourced from Beijing AMC Powder Metallurgy Technology Co., Ltd. The as-printed 316 L features a Young's modulus of approximately 190 GPa and a yield strength of around 520 MPa. The printing parameters governing the laser scanning path are summarized in Table S1. For the contour scanning path, the segment length (*SL*) varied from 5 μm to 400 μm, while the line hatch distance (*LHD*) ranged from 0 μm to 120 μm for each *SL*, resulting in 35 parameter combinations. A self-developed algorithm executed in MATLAB implements the whole process, including geometric modeling, slicing, and toolpath generation.

2.2. Characterization of manufacturing fidelity

The as-printed samples were subjected to ultrasonic cleaning following their removal from the build plate, which was performed using electrical discharge machining (EDM). The relative density of the lattice structures was calculated to assess the overall fidelity of the printing process. Shell thickness and surface quality were investigated by using the RH-2000 High-Resolution 3D Optical Microscope, HIROX. The average roughness, Ra, was evaluated through the depth reconstruction via the same microscope. The morphologies of the lattice samples were characterized by a scanning electron microscope (SEM, JCM-6000Plus). The crystal structure was characterized using an EBSD system (EDAX velocity Plus) with a step size of 0.2 μm, which was then analyzed using an open-source toolbox in MATLAB, MTEX. The Scanco Medical μCT-35 Micro-CT, featuring a 70 kV X-ray source, was utilized for non-destructive characterization, after which the rebuilt models were exported as STL files to furnish 3-dimensional geometric data.

2.3. Tensile and compression tests

Quasi-static compression tests were conducted using an MTS universal testing machine (Model 370.1, MTS Landmark® Testing Solutions). Young's modulus of the lattice was determined through cyclic loading-unloading compressive tests, calculated from the unloading curve slope[44]. Machine stiffness was calibrated via fixture compression to isolate the sample's intrinsic response; detailed procedures are provided in Supplementary Text 1. For the large deformation, a compression speed with a strain rate of 1.0×10^{-3} s^{-1} was applied until densification transpired. The yield stress, plateau stress, and energy absorption capability were utilized to evaluate the mechanical performance of the printed structures across the different path parameters[45]. Particularly, the yield strength of the lattice structures was ascertained by the 0.2% offset from the stress-strain curves.

In-situ synchrotron high-energy X-ray diffraction (HEXRD) tensile experiments were carried out at the FAST beamline of the Cornell High Energy Synchrotron Source using an X-ray energy of 67.416 keV (λ = 0.183 9 Å). The tensile tests were conducted at a nominal strain rate of 2.5×10^{-4} s^{-1}, and meanwhile, the two-dimensional X-ray diffraction patterns were collected in transmission mode with an X-ray beam size of 0.8 mm × 0.8 mm. We used the CeO_2 NIST powder standard to calibrate the sample-to-detector distance and instrumental broadening. One-dimensional diffraction patterns were acquired by integrating along the loading direction (±5)° using the GSAS-II software suite[46].

2.4. Numerical modeling of mechanical response

Finite element modeling is performed to simulate the effect of roughness on the deformation behavior of thin walls. Surface roughness is represented using Gaussian distributions based on root mean square (RMS) values[47], which are obtained from the experimental measurements. To capture the role of microstructural features in the mechanical response, crystal plasticity finite element simulations were performed using the OXFORD-UMAT framework[48]. Crystal characteristics, including grain boundaries and orientations, were extracted from electron backscatter diffraction (EBSD) data using the MTEX toolbox. The finite element mesh was then generated using the MTEX2Gmsh toolkit[49] (Figure S2). The total mechanical deformation gradient can be decomposed into two parts: the plastic deformation gradient and the elastic deformation gradient, which correspond to the irreversible plastic slip on active slip systems and reversible stretching and rotation of the crystal lattice, respectively. The power law slip is employed to compute the slip rates using resolved shear stress (RSS) as the driving force and critical resolved shear stress (CRSS) as the threshold for slip[48]. Then, the Voce-type hardening is used to evaluate the self-strain hardening rate of a slip system[48]. The parameters used in the simulation are provided in Table S2.

2.5. Molten pool modeling

The laser additive manufacturing process is simulated using a finite element model. Before the melting process, the powder layer was generated by the discrete element method[50,51]. The fluid is assumed to be incompressible, laminar, and Newtonian. The laser energy is converted into a heat source with Gaussian spatial distribution when the laser acts on the powder layer. Consequently, the powder temperature rises and transfers heat to the surrounding powder area due to the temperature difference. The energy is mainly dissipated outward using heat conduction and thermal radiation. The equations[52] governing mass, momentum, and energy conservation are:

$$\frac{\partial \rho}{\partial t} + \nabla \cdot \left(\rho \vec{V}\right) = M_s \tag{1}$$

$$\rho\left(\frac{\partial \vec{V}}{\partial t} + \vec{V} \cdot \nabla \vec{V}\right) = \mu \nabla^2 \vec{V} - \nabla P + M_s \cdot \vec{V} + F \tag{2}$$

$$\rho C_p \frac{\partial T}{\partial t} + \rho C_p \mu \cdot \nabla T = \nabla \cdot (\kappa \nabla T) + S_H. \tag{3}$$

The Equations (1)–(3) are mass conservation equations, momentum conservation equations, and energy conservation equations, respectively, and ρ, κ, μ, and P denote the density, thermal conductivity, dynamic viscosity, and pressure, respectively. C_p is the specific heat at the pressure, $\vec{V}$ is the motion velocity of the laser beam, M_s is a mass source, F is the body force, and S_H represents the source item of the energy equation[52]:

$$S_H = -\rho\left[\frac{\partial}{\partial t}\Delta H + \nabla\cdot\left(\vec{V}\Delta H\right)\right] \tag{4}$$

where ΔH is the latent heat of phase change. The parameters used in the simulation are provided in Table S3.

2.6. Thermal performance test

The compact cold plates were printed using pure copper powders. The alumina high-temperature ceramic heating element (100 W, 20 mm × 20 mm × 2 mm) serves as the heat source. Water at 27 °C is selected as the fluid medium and is conveyed into the cooling plate by the membrane pump at a volumetric flow rate of 200 mL·min^{-1}. A differential pressure transmitter (accuracy: ±0.1%) measures pressure changes, while PT100 thermocouples (accuracy: (±0.1) °C) measure temperature changes. Each parameter is measured three times, and the average value is recorded as the result.

3. Results and discussion

3.1. Concept of STL-free hybrid toolpath

Figure 1(a) schematically illustrates the toolpath engineering for the PBF-LB process. In PBF-LB, components are built by stacking molten pools layer by layer, a process that is directly influenced by the laser scanning path. To enhance this process, we developed an STL-free hybrid toolpath strategy tailored for shell-based microscale lattices, enabling improved shape fidelity, computational efficiency, and microstructural control. Figures 1(b)–(e) compare the traditional STL-based toolpath strategy and our STL-free hybrid path approach (Supporting information, Movie S1). In the traditional STL-based workflow, the R67 strategy, which involves rotating the scan path by 67° at successive layers, is widely used (Figure 1(b)). However, for curved thin-wall cellular structures, this generates numerous short paths that lead to rough surfaces, as shown in Figures 1(b-iii) and (b-iv). In contrast, our STL-free hybrid strategy differentiates between thin-wall regions and wall-joint regions, applying contour scanning to thin-wall areas and the R67 path only at wall joints. Figure 1(c) demonstrates how this hybrid approach produces smoother surfaces and addresses manufacturing challenges in thin-wall and overhang regions.

The high-fidelity hybrid path improves dimensional accuracy by reducing thickness deviations. Figures 1(d) and (e) show the cross-section of vertical walls printed with the R67 and hybrid paths. Walls printed using the R67 method exhibit more significant deviations and boundary fluctuations due to frequent path rotations and numerous lasers' start/end points. In contrast, walls printed with the hybrid path achieve better accuracy, with a consistent thickness of (65.3 ± 4.6) μm. Surface roughness is also reduced threefold (from 9.1 μm to 3.2 μm) along with a threefold decrease in thickness variation (from 14.6 μm to 4.6 μm, Figure S3). Beyond shape fidelity, the hybrid toolpath also refines microstructural features. As shown, crystallographic grains exhibit a more uniform size and orientation when the hybrid strategy is employed, further contributing to the enhanced mechanical properties of the printed structures (Figures 1(d-ii) and (e-ii)).

The STL-free hybrid toolpath strategy reduces computational demands by generating toolpaths directly from implicit TPMS functions. In conventional STL-based workflows, TPMS surfaces are first triangulated using the marching cubes algorithm, which has a computational complexity of $O(n^3)$, followed by slicing and path planning operations that collectively lead to an overall complexity of approximately $O(n^4)$. In contrast, the proposed method bypasses 3D triangulation entirely, directly generating toolpaths from the implicit functions with a computational complexity of $O(n^2)$. To quantify this improvement, a Gyroid-type TPMS lattice was analyzed under identical conditions (unit cell size: 2.5 mm; resolution: 0.01 mm), comparing the traditional STL-based approach (implemented via open-source MATLAB code[39]) with the proposed STL-free hybrid toolpath strategy (Figure 1(f)). The proposed method reduced computational demands by over 90% relative to the STL-based technique, which exhibited exponential improvements in both time and memory consumption as lattice complexity increased (Table S4 and Figure S4).

3.2. One-stop solution: from function to path

The STL-free hybrid toolpath strategy seamlessly bridges the function-based implicit geometries and scanning paths, bypassing any STL-related steps to achieve superior computational capability and efficiency. Our focus is on thin-walled lattice structures, dividing regions into thin-wall and wall-joint areas. The toolpath generation process consists of three steps: direct slicing, region determination, and path generation.

To demonstrate the method, we selected TPMS, a commonly used class of implicit function-defined smooth surfaces (Figures 2(a) and (b)). The geometry is described by a level-set function $\phi\,(x,y,z):\ R^3 \mapsto R$, which defines the 3D surface. Three types of TPMS surfaces were specified by equations provided in Supplementary Text 2[53]. The TPMS sheet models were created by enclosing two implicit surfaces, defined by Equation (5).

$$\Phi\,(x,y,z) = \phi_{IS}^2\,(x,y,z) - c^2\,(x,y,z) \tag{5}$$

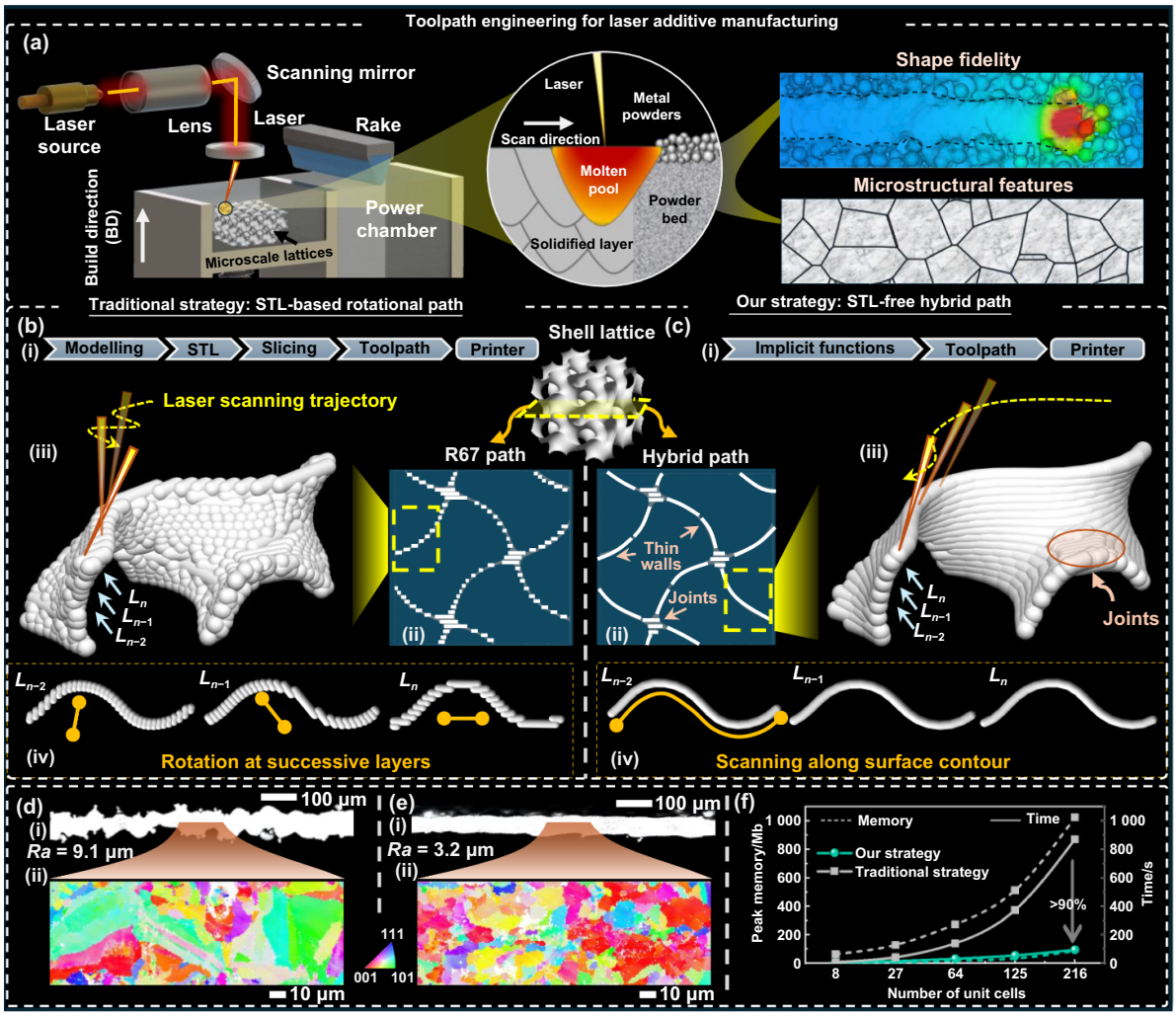

Figure 1. Toolpath engineering for laser additive manufacturing. (a) Schematic of PBF-LB system, printing configuration, resulting shape, and microstructures. (b) Traditional STL-based strategy. (c) Our proposed STL-free hybrid strategy. In (b) and (c), (i) digital workflow of different strategies; (ii) schematic diagram of the planned path; (iii) schematic diagram of shell lattice surfaces fabricated via two scanning strategies; (iv) schematic diagram of scanning path at three layers. (d) and (e) The dimensional accuracy and microstructural features of shell lattice printed via two strategies. In (d) and (e), (i) cross-sections of as-printed thin walls; (ii) electron backscatter diffraction (EBSD) inverse pole figure (IPF) maps showing crystal grain orientations at the top surface. (f) Consumption of peak memory and time of two strategies for generating the G-type TPMS structures with various cells. Time and peak memory are evaluated in MATLAB R2020a using a 2.2 GHz Intel 4210 with 128 GB of memory.

$$\vec{n}(x,y,z) = \left[\frac{\partial \phi_{IS}}{\partial x}, \frac{\partial \phi_{IS}}{\partial y}, \frac{\partial \phi_{IS}}{\partial z}\right] \tag{6}$$

Where ϕ_{IS} is the governing function for the implicit surfaces. $c(x,y,z)$ is the scale value to control the thickness of the sheet, which can be adjusted independently at the point of (x,y,z), $\vec{n}$ is the normal vector of the middle surface at the point of (x,y,z). The slicing process generates intersection curves or contours by solving the level-set equation:

$$\Phi(x,y,z_i) = 0. \tag{7}$$

Where z_i is the z coordinates at the i^{th} slicing layer.

Figures 2(a) and (b) illustrate the level-set values and resulting contours for given layers. Thin-wall and wall-joint regions are separated based on the inclination angle of the middle surface, derived from the normal vector, $\vec{n}(x,y,z)$, as defined by Equation (6). For areas with an inclination angle below a threshold, the variable $c(x,y,z)$ remains constant; however, for higher angles, $c(x,y,z)$ is set to zero, and interpolation generates a new c-value distribution (Figure S5). Boolean subtraction is then applied to trim the initial contours (Figure 2(a-ii)), producing the final scanning regions (Figure 2(a-iii)).

In the next step, scanning paths are generated for both regions. The contour path is derived directly from contours, using a high-resolution mesh to represent the geometry with small line segments. Adjustments to the length of segments (LS) and line hatch distance (LHD) help mitigate thermal stresses and reduce unwanted powder sintering (Figure 2(a-iv)). Shifting path segments between layers minimizes defects caused by thermal stress accumulation at laser start/end points

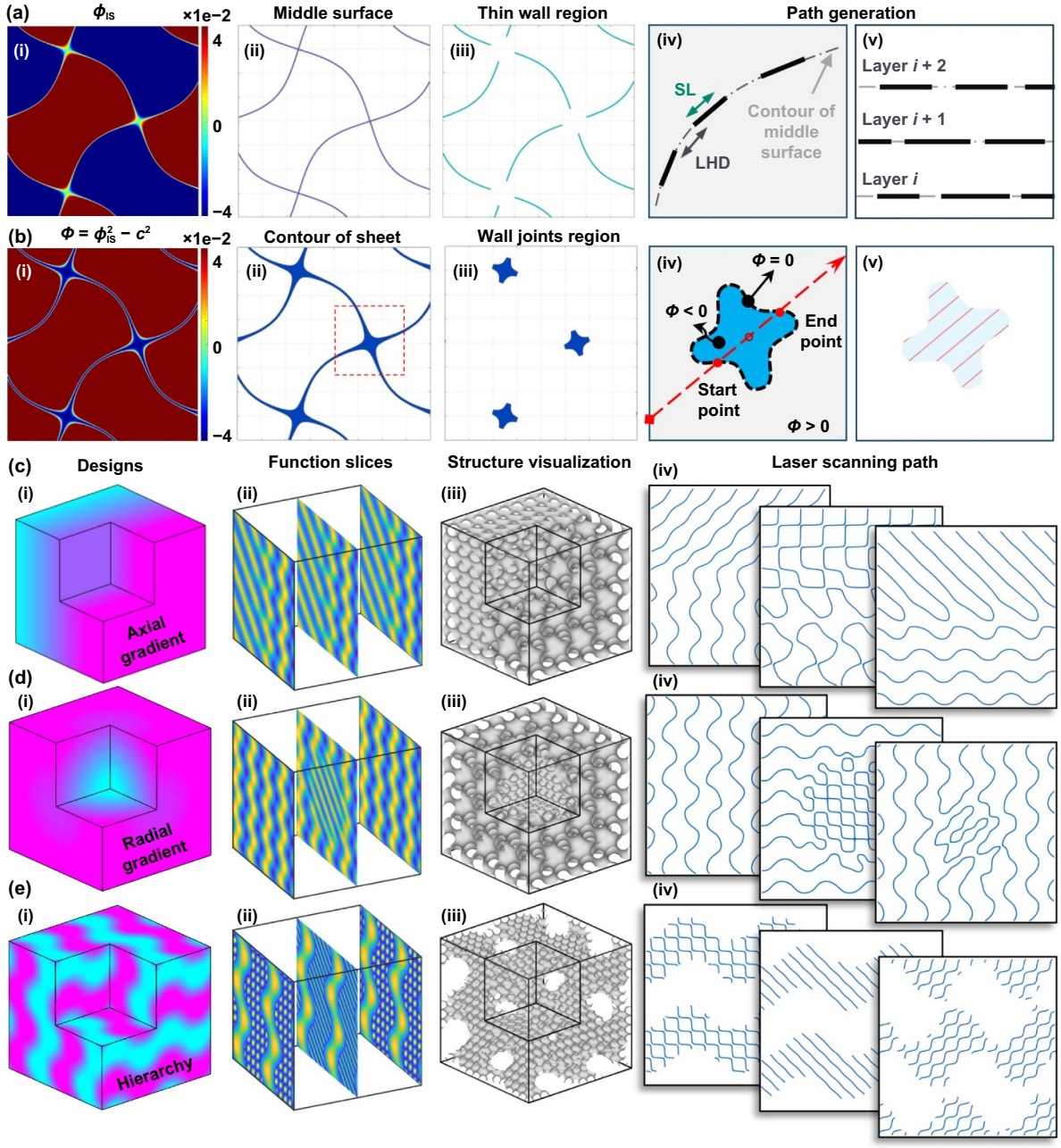

Figure 2. Illustration of the path generation process and applications on different shell lattice structures. (a) Contour path generated from implicit functions. In (a), (i) level-set value of function; (ii) cross section of middle surface; (iii) thin wall regions; (iv) parameter of contour scanning path; (v) shift at successive layers. (b) R67 path generated from implicit functions. In (b), (i) level-set value of the function; (ii) cross section of shell; (iii) wall joint region; (iv) toolpath generation of R67 based on functions; (v) R67 path. (c)-(e) Implicit function defined geometries with axial gradient, radial gradient, and hierarchical structures. In (c)-(e), (i) illustration of weighting functions; (ii) level-set value of functions; (iii) visualized 3D structures; (iv) scanning path.

(Figure 2(a-v)). For wall-joint regions, intersection points are identified by locating zeros of the implicit functions. As shown in Figures 2(b-iv) and (b-v) based on the scanning direction and boundary, step sizes are selected to search for line segments containing zero points. The laser spot diameter is used as a compensation factor to generate the scanning path.

To showcase the advantages of the STL-free hybrid toolpath strategy, we designed and fabricated axial, radial gradient, and hierarchy shell lattice structures (Figures 2(c)–(e)). Using the Sigmoid function, smooth transitions between different lattice materials were achieved. Hierarchical structures were directly generated by manipulating the implicit

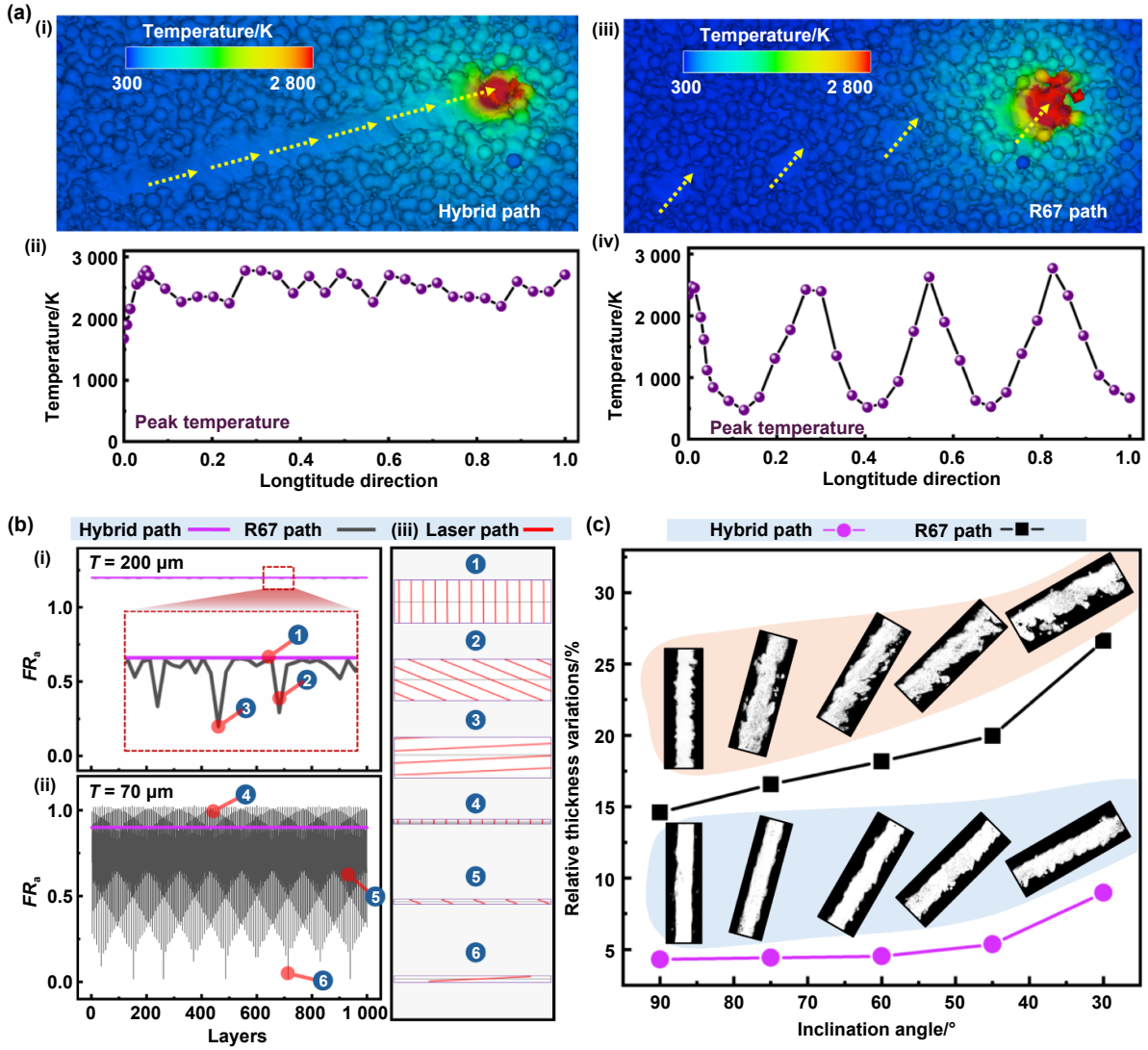

Figure 3. Manufacturability of thin walls. (a) Numerical simulation of temperature field and peak temperature along the wall's longitude direction during the laser additive manufacturing process. In (a), (i) and (ii) hybrid path; (iii) and (iv) R67 path. (b) Stability of filling ratio. In (b), (i) thick wall with a thickness of 200 μm; (ii) thin wall with a thickness of 70 μm; (iii) laser scanning tracks of R67 path. (c) Morphology of as-printed thin-walls and corresponding relative thickness deviations at different inclination angles.

functions, with laser scanning paths derived directly from these geometries.

3.3. Manufacturability and printing fidelity of microscale lattices

Fabricating high-resolution microscale lattice structures using laser additive manufacturing presents unique challenges, particularly when feature sizes approach the dimensions of the molten pool. In these conditions, the laser input energy density becomes critical in determining the thermal history and structural integrity of the printed components. Numerical results show that the hybrid toolpath ensures a stable energy input with low fluctuations and more uniform temperature distribution along thin walls (Figure 3(a)). Notably, results demonstrate that the classical criterion of volumetric energy input density[54] is unsuitable for ultra-thin wall structures. To address this, we introduce the filling ratio of area, FR_a, as a metric to quantify the influence of geometry on energy input density across successive layers, expressed as:

$$FR_a = \frac{D \cdot \sum \widetilde{L}_p}{A} \tag{8}$$

Where D is the molten pool width, measured as (63.8 ± 2.7) μm, $\widetilde{L}_p$ is the equivalent length of laser scanning path (Supporting information, Text 3), and A is the area of the planning region. The filling ratio directly correlates with energy input density in thin-wall structures.

We analyzed FR_a fluctuations in two thin walls over 1 000 layers using a hatch distance of 40 μm and beam compensation of 30 μm. For thicker walls, both the R67 and hybrid paths exhibit comparable filling ratios with minimal variation (Figure 3(b-i)). However, when the scanning direction becomes nearly parallel to the wall, the filling ratio drops.

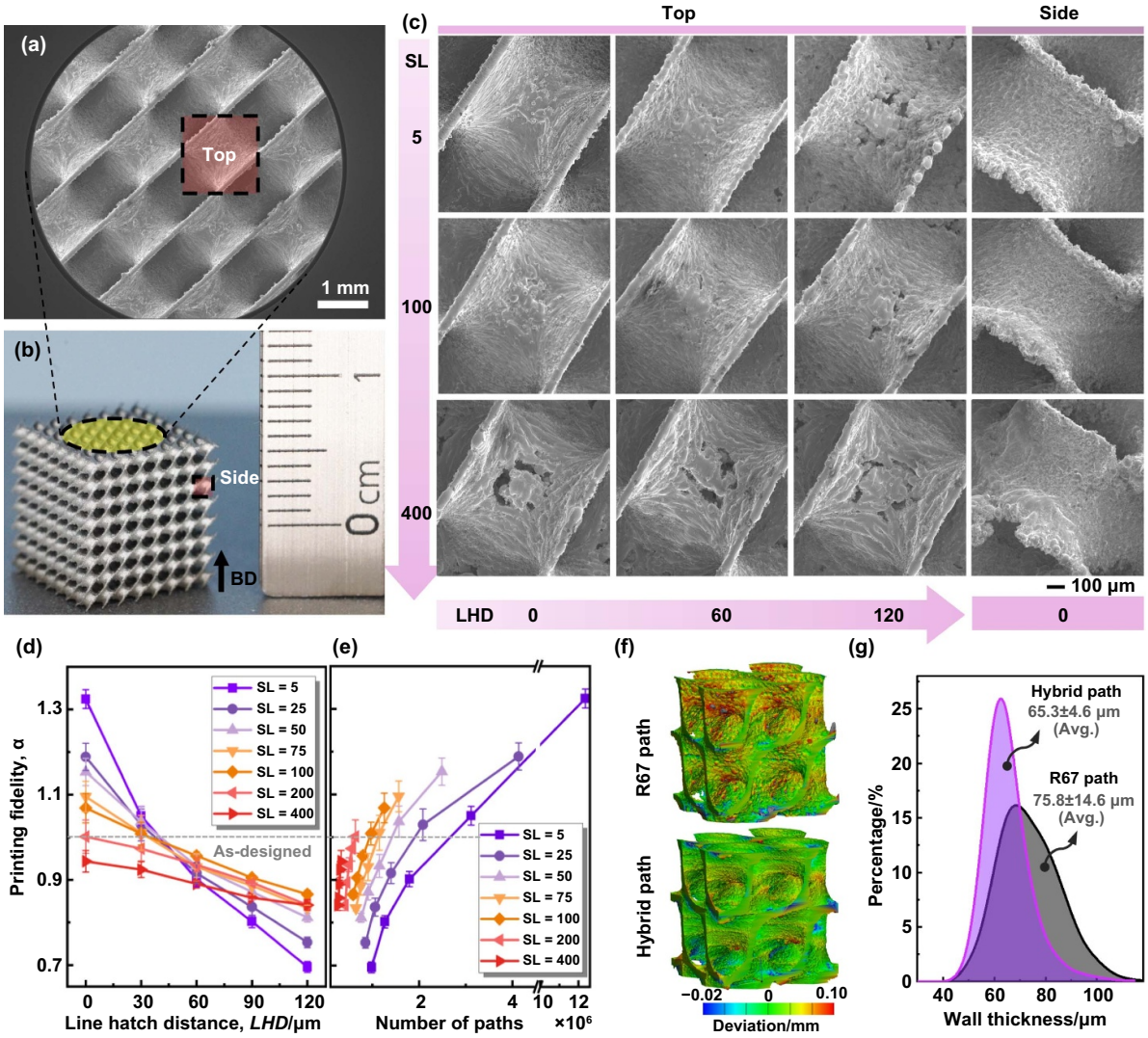

Figure 4. Effect of printing parameters on the manufacturing fidelity. (a) and (b) As-printed D-type TPMS lattice structure. (c) Morphology of as-printed lattices under different toolpath parameters. (d) Effects of *SL* and *LHD* on manufacturing fidelity. (e) Effect of the number of scanning paths on manufacturing fidelity. (f) 3-dimensional deviations. (g) Distribution of wall thickness.

For 70 μm thin walls, the R67 path exhibits large FR_a variations across layers, with values dropping from 103% to as low as 1.7% in some layers, compromising structural integrity. In contrast, the hybrid path maintains a consistent FR_a (Figure 3(b-ii)). The corresponding laser scanning tracks of the R67 path are schematically illustrated in Figure 3(b-iii). Fluctuations in FR_a are particularly pronounced when printing thin, inclined walls, leading to substantial deviations in wall thickness. For vertical walls, the R67 path results in deviations 2.3 times greater than those observed with the hybrid path, with deviations worsening as overhang angles decrease (Figure 3(c)). While the steady-state model used in this work clarifies energy density differences between toolpath strategies, it does not consider transient thermal effects, such as non-uniform heat accumulation or remelting, which are driven by dynamic laser scan directions. Notably, laser absorptivity and molten pool stability are highly sensitive to scan angles and toolpath continuity. In contour/R67 transition zones, abrupt changes in thermal boundaries and residual stress fields may promote defect formation (e.g., microcracks, porosity) and distortion. In future work, we will integrate transient thermo-fluidic modeling into the current framework to quantify these effects in different toolpath strategies.

The effect of path parameters on printing quality is studied using a D-type TPMS shell lattice with a 2.5 mm cell size and a 4 × 4 × 4 tessellation configuration (Figures 4(a) and (b)). Reducing *SL* and *LHD* significantly improves surface quality (Figure 4(c)). Large holes appear at $LHD = 0$ μm and $SL = 400$ μm due to inaccuracies in representing curved contours, particularly in areas with high curvature. Printing fidelity, α, is evaluated using the relative density (*RD*) ratio, defined as: $RD_{printed}/RD_{designed}$, which varies depending on *SL* and *LHD*. The highest *RD* is achieved at the smallest $SL = 5$ μm and $LHD = 0$ μm, while the lowest *RD* occurs at the same *SL* but with $LHD = 120$ μm (Figure 4(d)). *RD* decreases as *LHD* increases, with the rate of decrease depending on *SL*. The smallest *SL* (5 μm) shows the steepest decline, attributed to the reduced line-filling ratio, defined as $SL/(SL + LHD)$.

The number of paths also significantly affects the weight and *RD*. A reduced number of paths correlates with lower RD values, likely due to fewer laser start/end points. This reduction minimizes the heat-affected zone, thereby limiting the accumulation of excess sintered powder particles (Figure 4(e)). Micro-CT analysis reveals that the hybrid path produces walls with an average thickness of (65.3 ± 4.6) μm, compared to (75.8 ± 14.6) μm for the R67 path (Figures 4(f) and (g)). The hybrid path also achieves a 68% reduction in thickness variation, resulting in more uniform wall thickness.

3.4. Superior mechanical performance enabled by toolpath engineering

The surface roughness of PBF-LB fabricated components, combined with unique microstructural characteristics, plays a critical role in determining the mechanical performance of metallic shell-based lattice architectures. To study this, finite element modeling (FEM) is performed to simulate the effect of roughness on the deformation behavior of thin walls. Surface roughness is represented using Gaussian distributions based on root mean square (RMS) values[47]. As shown in Figure 5(a), increased roughness results in non-uniform stress distribution, with some regions bearing little to no load (Figure 5(a-i)), leading to stress concentration and reduced load-bearing efficiency. For example, at 2.5% macro strain, high-roughness samples exhibit low-strain regions (local strain <10% of macro strain) encompassing 16.3% of the material volume, compared to just 4.1% in low-roughness samples (Figure 5(a-ii)). Surface roughness critically governs mechanical behavior, with yield strength declining by 17% (from 510 MPa to 425 MPa) and effective wall thickness diminishing by 16% (from 73 μm to 61 μm) as roughness intensifies from 3 μm to 8 μm (Figure 5(a-iii)).

The deformation behavior of thin-wall structures is further investigated using in-situ synchrotron high-energy X-ray diffraction (HEXRD) under uniaxial tension, providing insights into the evolution of crystallographic lattices. Figure 5(b) shows that the hybrid toolpath achieves superior mechanical performance, with higher strength and enhanced ductility compared to the R67 path. Both specimens initially displayed a (111) diffraction peak at approximately 5.067°. Under applied tension, the hybrid toolpath specimen exhibited a uniform progressive shift of the peak toward lower diffraction angles, indicating a more homogeneous strain distribution. In contrast, the R67 path sample shows pronounced peak splitting near fracture, with two distinct peaks at 5.042 and 5.067 degrees (Figure 5(b-iii)). This peak separation suggests the presence of considerably undeformed regions due to the higher surface roughness and smaller effective thickness for the R67 path sample. This means the effective thickness of the shell wall involved in deformation is notably smaller than the measured value.

Microstructural analysis (Figure 5(c)) elucidates the differences between the hybrid and R67 toolpath. The hybrid toolpath generates a more uniform grain size distribution in the top view and reduces crystal misorientation in the side view compared to the R67 path. Despite these differences, experimental results indicate that both toolpath strategies produce thin walls with anisotropic mechanical properties (Figure S6). Specifically, the yield strength along the build direction remains approximately 15% lower than that along the horizontal direction, irrespective of the toolpath strategy, suggesting that the degree of anisotropy is unaffected by toolpath engineering. Notably, the hybrid toolpath achieves refined and uniformly distributed grains, showing an improvement in yield strength of approximately 10% compared to the R67 path. Quantitative EBSD analysis reveals that the 53 MPa yield strength improvement achieved through the hybrid toolpath strategy stems primarily from grain boundary and dislocation strengthening. By applying the Hall-Petch[55] relationship and the Bailey-Hirsch[56] model, we attribute roughly 26.2 MPa and 23.7 MPa of this enhancement to grain refinement and increased dislocation density as the two main strengthening mechanisms (Supplementary Text 3). Furthermore, crystal plasticity finite element (CPFE) simulation results further support these experimental observations, demonstrating that the hybrid toolpath promotes a more homogeneous strain distribution. This improved strain uniformity reduces stress concentrations, thereby enhancing both strength and toughness[57,58].

The mechanical property improvements are even more pronounced in TPMS lattice samples, which are highly sensitive to manufacturing defects under tensile loading-unloading (Figure 5(d)). Both tensile yield strength and ultimate tensile strength show significant increments via laser toolpath engineering. The hybrid path samples exhibit a yield strength and ultimate strength of 27.6 MPa and 42.0 MPa, respectively, significantly higher than the R67 path values of 16.6 MPa and 18.9 MPa, representing increases of 66% and 122% (Figure 5(d-i)). Damage evaluation, measured by stiffness degradation ($D = 1 - E/E_0$, where E is the elastic modulus during loading and E_0 is the initial elastic modulus), further highlights the hybrid path's advantages (Figure 5(d-ii)). Hybrid path samples exhibit much slower damage accumulation, reaching $D = 0.2$ after 26 loading-unloading cycles, compared to just 7 cycles for the R67 path. Fracture surface analysis reveals that R67 samples contain numerous voids caused by surface roughness and defects, accelerating crack initiation and propagation (Figures 5(d) and S7). In contrast, the hybrid path significantly enhances the durability and fatigue resistance of the structures by mitigating crack growth (Figure S8). Importantly, the fatigue performance of lattice structures is often more sensitive to surface imperfections than to the bulk parts[14]. Surface depressions resulting from the rough as-built surface can act as effective micro-notches, significantly reducing fatigue life, particularly when their dimensions are comparable to the shell thickness. Under compression-compression fatigue testing, cracks are frequently observed to initiate either from internal voids or from surface sites prone to mode-I cracking[59]. The improved surface quality achieved by the proposed strategy is therefore expected to significantly enhance fatigue resistance by mitigating crack initiation

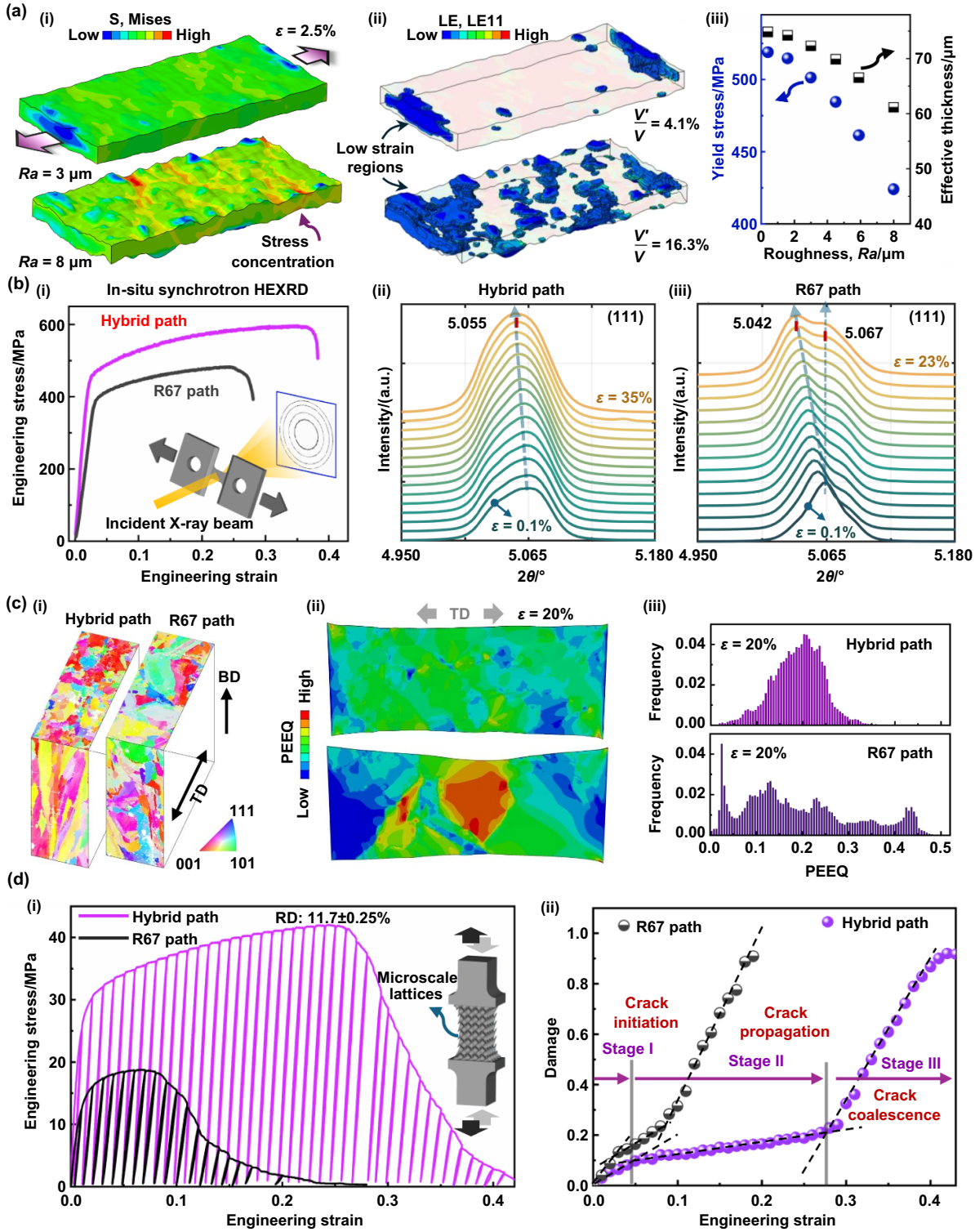

Figure 5. Mechanical responses of as-built thin walls and microscale lattices. (a) FEM simulations of thin wall tensile tests with different surface roughness. In (a), (i) the stress distribution; (ii) the low-strain regions; (iii) the effect of surface roughness on the yield stress and effective thickness. (b) In-situ synchrotron HEXRD testing results. In (b), (i) stress-strain curves; (ii)-(iii) diffraction pattern with increasing strain. (c) Effect of microstructural features. In (c), (i) EBSD IPF maps showing the grain orientation at top and side surfaces, corresponding to the building direction (BD) and horizontal tensile direction (TD), respectively; (ii)-(iii) PEEQ distribution map and its frequency distribution obtained from CPFE simulation results at 20% tensile strain. (d) Toughness of lattice structures fabricated via two strategies. In (d), (i) engineering stress-strain curves under tensile loading-unloading cycles; (ii) damage evolution.

sites, thereby extending the service life of TPMS lattice structures. Relevant studies[14,60] have shown that surface finishing and defect reduction can lead to substantial improvements in fatigue performance, underscoring the importance of our approach for applications requiring long-term durability.

The scalability of the hybrid toolpath was tested by printing lattice structures with varying cell sizes across a wide range of *RD*. Using the Gibson and Ashby framework[61], the relative yield strength (σ/σ_s) and energy absorption capacity (W/σ_s) were analyzed for different lattice configurations following the equations:

$$\frac{\sigma}{\sigma_s} = C_1\rho^{n_1}; \frac{W}{\sigma_s} = C_2\rho^{n_2} \tag{9}$$

where σ_s is the yield stress of the bulk material, ρ is the *RD* of lattices. The coefficients C and n differ depending on the lattice types, material, or manufacturing method. The hybrid path consistently outperforms the R67 path, with improvements in both yield strength and energy absorption, especially at lower relative densities (Supplementary Figure 9). Thus, it can be demonstrated that the hybrid strategy achieves feature sizes as small as 65 μm without compromising mechanical properties.

The mechanical performance of our lattices was compared with published experimental data and theoretical strength bounds (Suquet and Voigt upper bound[62]) for cellular materials. As shown in Figure S9(b), our lattices achieve 40%–65% of the Suquet limit at a large relative density range of 5%–25%, surpassing prior experimental results by over 35% in low-density regimes ($\rho < 10\%$). Conventional methods exhibit rapid strength degradation in these regimes, with deviations from theoretical predictions by >80% at $\rho = 5\%$. This discrepancy likely arises from manufacturing defects (e.g., porosity, surface roughness) that disproportionately compromise the mechanical integrity of slender truss/shell with high-aspect-ratio in low-density lattices. Moreover, heat treatment was conducted to assess its impact on mechanical properties. At 650 °C for 2 hours[63] (HT-650), yield strength and energy absorption increased by 3.8% and 10.6%, respectively. In contrast, treatment at 950 °C[63] (HT-950) resulted in decreases of 10% and 1%. These changes may stem from dispersion strengthening at lower temperatures and cellular structure dissolution at higher temperatures (Figure S10), as extensively discussed in previous studies[56,64].

While the toolpath strategy demonstrates efficacy with 316L stainless steel, chosen for its good printability and stability, material-specific constraints may arise. For instance, difficult-to-print materials like pure copper (high reflectivity, thermal conductivity) or high-entropy alloys (low ductility, crack susceptibility) may not achieve comparable resolution. Additionally, materials sensitive to microstructural anisotropy could exhibit heightened directional property variations. To ensure robust mechanical performance and printing quality across diverse materials, further toolpath parameter optimization is required.

4. Applications and validations

Additive manufacturing offers unprecedented design freedom to fully explore the superior performance of lattice structures. Here, we highlight some potential applications of microscale metallic lattice structures in lightweight design and thermal management—areas that require high resolution and excellent surface finish, where the hybrid toolpath holds its unique advantages.

In aerospace engineering, reducing component weight without sacrificing structural integrity is a key design goal. Lattice-based geometries are particularly well-suited for this purpose, providing excellent stiffness-to-weight ratios. To showcase the effectiveness of our hybrid toolpath strategy, we fabricated the GE bracket, a benchmark case for a lightweight design, using both the conventional R67 approach and the hybrid toolpath strategy. The brackets incorporated a TPMS lattice (unit cell size: 2.5 mm, >1 000 cells) through Boolean operations[41], ensuring the preservation of functional connection features like screw holes and joints (Figure 6(a-i)).

The hybrid toolpath significantly improves surface quality, reducing roughness from 8.3 μm to 2.8 μm and minimizing porosity in the solid concurrently (Figures 6(a-ii) and (a-iii)). These improvements translate to superior mechanical performance, with the bracket achieving a 52% increase in ultimate tensile strength compared to the R67 path. Toughness also improves dramatically, with energy absorption before failure increasing fivefold from 0.32 J (R67 path) to 1.72 J (Figure 6(a-iv)). This performance boost underscores the critical role of surface quality in lattice structures, enabled by precise toolpath engineering. In addition, the hybrid strategy reduces fabrication time per layer by 38.6%–50% (Movie S2). This efficiency gain is even more pronounced in microscale lattices with smaller unit cells.

The hybrid path also excels in thermal management, essential for industries like high-performance electronics and energy conversion systems. Fabricating complex heat management components, such as cold plates, is often challenging due to geometric complexity. The hybrid toolpath strategy addresses this challenge, enabling the production of intricate freeform lattice structures with superior heat transfer performance. For example, we fabricated a microscale shell lattice cold plate from pure copper (25 mm × 25 mm × 6.2 mm, unit cell size: 1.5 mm, ∼1 100 cells). To assess cooling performance, a 100 W heat source was used, with water pumped through the cold plate (Figures 6(b-i) and (b-ii)). Lattice-based cold plates utilizing hybrid and R67 paths demonstrate superior cooling performance compared to traditional tube designs, achieving 60% and 20% higher cooling rates, respectively, despite slightly higher pressure drops (Figures 6(b-ii) and (b-iii)). This improvement arises from optimized flow dynamics: interconnected curved channels in TPMS lattices minimize flow stagnation via multi-scale fluid redistribution, while vortices disrupt thermal boundary layers[65–67]. Enhanced helical flows circulate heated fluid from walls to the core while drawing

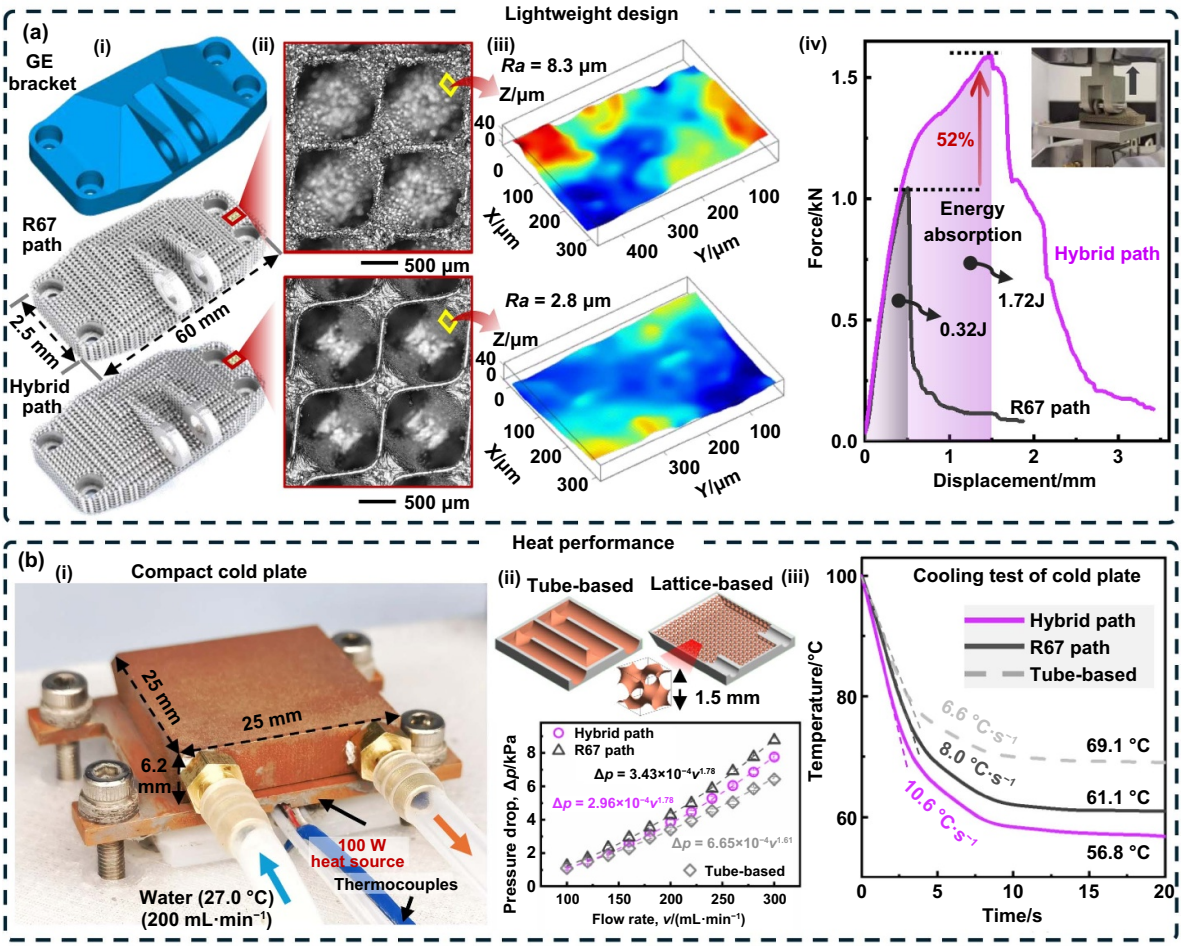

Figure 6. Multi-disciplinary applications. (a) Lattice-based lightweight design. In (a), (i) lattice-filled GE bracket printed by the R67 path and hybrid path; (ii) and (iii) morphology and surface roughness of lattice structures; (iv) Force-displacement curves during tensile test. (b) Thermal performance test of compact cold plate. In (b), (i) experimental setup; (ii) the configurations of tube-based and lattice-based cold plate, and pressure drop at different flow rates; (iii) temperature response during the cooling process.

cooler fluid toward heated surfaces, promoting self-sustaining thermal mixing[65,66].

Surface roughness exerts dual effects: heat transfer increases over surface roughness peaks due to flow impingement, acceleration, and enhanced conductive pathways, but decreases in valleys where low-velocity flow thickens thermal boundary layers[68]. Overall, heat transfer gains dominate due to the net positive impact of roughness peaks[68,69]. However, roughness elevates pressure drop through the form drag (projection of roughness elements) and viscous drag (fluid shear stress)[68].

Lattice channels with reduced roughness mitigate these trade-offs. Their helical flow patterns reduce stagnation zones and minimize drag, achieving efficient heat transfer with limited pressure drop penalties. Notably, pressure drop differences become critical at low flow rates (as evidenced by the exponent relationship in Figure 6(b-ii)), underscoring the value of compact lattice designs that tailor flow behavior to maximize thermal efficiency.

5. Conclusion

This work presents an STL-free hybrid toolpath strategy that directly converts implicit lattice models into optimized laser scanning paths, eliminating computational bottlenecks and significantly enhancing mechanical performance. By bypassing intermediate STL mesh, the method achieves a 90% reduction in memory usage and processing time, while enabling the high-fidelity fabrication of microscale shell lattices with a 66% increase in yield strength and 257% improvement in elongation. Experimental and numerical analyses reveal the critical role of surface quality and microstructural control in governing mechanical behavior, emphasizing the transformative impact of toolpath engineering. Furthermore, cyclic loading tests and fracture morphology studies highlight the potential of this approach for applications demanding long-term durability. Future work will focus on extending this strategy toward microstructure-tailored architectures through spatially graded toolpath modulation, further circumventing

advancing the design and fabrication of next-generation architected metamaterials.

Acknowledgments

The authors acknowledge the financial support of the Hong Kong Special Administrative Region University Grants Committee—General Research Fund CUHK14209523 as well as Collaborative Research Fund C4074-22G, C4002-22Y and C7074-23G. W.C. acknowledges the faculty start-up support by the University of Massachusetts Amherst.

Conflict of interests

The authors declare no competing interests.

ORCID iDs

Junhao Ding 0000-0001-8643-7518
Chinnapat Panwisawas 0000-0003-2141-5865
Wen Chen 0000-0003-2048-1107

References

[1] Zheludev N I and Kivshar Y S. 2012. From metamaterials to metadevices. *Nat. Mater.* **11**, 917–924.
[2] Qi J X et al. 2022. Recent progress in active mechanical metamaterials and construction principles. *Adv. Sci.* **9**, 2102662.
[3] Ma W W S et al. 2025. Multi-physical lattice metamaterials enabled by additive manufacturing: design principles, interaction mechanisms, and multifunctional applications. *Adv. Sci.* **12**, 2405835.
[4] Sirote-Katz C, Shohat D, Merrigan C, Lahini Y, Nisoli C and Shokef Y. 2024. Emergent disorder and mechanical memory in periodic metamaterials. *Nat. Commun.* **15**, 4008.
[5] Zhang H, Wu J, Fang D N and Zhang Y H. 2021. Hierarchical mechanical metamaterials built with scalable tristable elements for ternary logic operation and amplitude modulation. *Sci. Adv.* **7**, eabf1966.
[6] Fang X, Wen J H, Cheng L, Yu D L, Zhang H J and Gumbsch P. 2022. Programmable gear-based mechanical metamaterials. *Nat. Mater.* **21**, 869–876.
[7] Liu Y, Wang Y Z, Ren H Y, Meng Z Q, Chen X Q, Li Z Y, Wang L W, Chen W, Wang Y F and Du J B. 2024. Ultrastiff metamaterials generated through a multilayer strategy and topology optimization. *Nat. Commun.* **15**, 2984.
[8] Yang Y H et al. 2022. Gaussian curvature–driven direction of cell fate toward osteogenesis with triply periodic minimal surface scaffolds. *Proc. Natl Acad. Sci. USA* **119**, e2206684119.
[9] Zeng Q L, Duan S Y, Zhao Z A, Wang P D and Lei H S. 2023. Inverse design of energy-absorbing metamaterials by topology optimization. *Adv. Sci.* **10**, 2204977.
[10] Zhou S X, Zhao Y J, Zhang K X, Xun Y R, Tao X Y, Yan W T, Zhai W and Ding J. 2024. Impact-resistant supercapacitor by hydrogel-infused lattice. *Nat. Commun.* **15**, 6481.
[11] Blakey-Milner B, Gradl P, Snedden G, Brooks M, Pitot J, Lopez E, Leary M, Berto F and du Plessis A. 2021. Metal additive manufacturing in aerospace: a review. *Mater. Des.* **209**, 110008.
[12] Koons G L, Diba M and Mikos A G. 2020. Materials design for bone-tissue engineering. *Nat. Rev. Mater.* **5**, 584–603.
[13] Jiao P C, Mueller J, Raney J R, Zheng X Y and Alavi A H. 2023. Mechanical metamaterials and *beyond*. *Nat. Commun.* **14**, 6004.
[14] Benedetti M, du Plessis A, Ritchie R O, Dallago M, Razavi N and Berto F. 2021. Architected cellular materials: a review on their mechanical properties towards fatigue-tolerant design and fabrication. *Mater. Sci. Eng. R* **144**, 100606.
[15] du Plessis A, Razavi N, Benedetti M, Murchio S, Leary M, Watson M, Bhate D and Berto F. 2022. Properties and applications of additively manufactured metallic cellular materials: a review. *Prog. Mater. Sci.* **125**, 100918.
[16] Ding J H, Ma Q P, Li X W, Zhang L, Yang H, Qu S, Wang M Y, Zhai W, Gao H J and Song X. 2024. Imperfection-enabled strengthening of ultra-lightweight lattice materials. *Adv. Sci.* **11**, 2402727.
[17] Gu D D, Shi X Y, Poprawe R, Bourell D L, Setchi R and Zhu J H. 2021. Material-structure-performance integrated laser-metal additive manufacturing. *Science* **372**, eabg1487.
[18] Sun X Y, Chen M N, Liu T T, Zhang K, Wei H L, Zhu Z G and Liao W H. 2024. Characterization, preparation, and reuse of metallic powders for laser powder bed fusion: a review. *Int. J. Extrem. Manuf.* **6**, 012003.
[19] Liu G et al. 2021. Additive manufacturing of structural materials. *Mater. Sci. Eng. R* **145**, 100596.
[20] Feng J W, Fu J Z, Yao X H and He Y. 2022. Triply periodic minimal surface (TPMS) porous structures: from multi-scale design, precise additive manufacturing to multidisciplinary applications. *Int. J. Extrem. Manuf.* **4**, 022001.
[21] Yuan B, Wang L, Zhao R, Yang X, Yang X, Zhu X, Liu L, Zhang K, Song Y and Zhang X. 2020. A biomimetically hierarchical polyetherketoneketone scaffold for osteoporotic bone repair. *Sci. Adv.* **6**, eabc4704.
[22] Ma S et al. 2020. Manufacturability, mechanical properties, mass-transport properties and biocompatibility of triply periodic minimal surface (TPMS) porous scaffolds fabricated by selective laser melting. *Mater. Des.* **195**, 109034.
[23] Fu J, Qu S, Ding J H, Song X and Fu M W. 2021. Comparison of the microstructure, mechanical properties and distortion of stainless steel 316 L fabricated by micro and conventional laser powder bed fusion. *Addit. Manuf.* **44**, 102067.
[24] Murr L F. 2017. Open-cellular metal implant design and fabrication for biomechanical compatibility with bone using electron beam melting. *J. Mech. Behav. Biomed. Mater.* **76**, 164–177.
[25] Guo A X Y, Cheng L, Zhan S, Zhang S, Xiong W, Wang Z, Wang G and Cao S C. 2022. Biomedical applications of the powder-based 3D printed titanium alloys: a review. *J. Mater. Sci. Technol.* **125**, 252–264.
[26] Wang Y F, Ji X and Liang S Y. 2023. Analytical modeling of temperature distribution in laser powder bed fusion with different scan strategies. *Opt. Laser Technol.* **157**, 108708.
[27] Li H K, Brodie E G and Hutchinson C. 2023. Predicting the chemical homogeneity in laser powder bed fusion (LPBF) of mixed powders after remelting. *Addit. Manuf.* **65**, 103447.
[28] Qin M, Ding J H, Qu S, Song X, Wang C C L and Liao W H. 2024. Deep reinforcement learning based toolpath generation for thermal uniformity in laser powder bed fusion process. *Addit. Manuf.* **79**, 103937.
[29] Wu C C, Zafar M Q, Zhao H Y, Wang Y, Schöler C, Heinigk C, Nießen M and Schulz W. 2021. Multi-physics modeling of side roughness generation mechanisms in powder bed fusion. *Addit. Manuf.* **47**, 102274.
[30] Vivegananthan P, Gao S B, Ji W M, Fan H Y, Han C J and Zhou K. 2024. Recent progress on 3D printing of lightweight metal thin-walled structures. *Adv. Mater.* **36**, 2402130.
[31] Jiang M L, Yang Y, Han C, Liu J, Yan M, Yang C, Wei S, Lu H and Wang D. 2024. Defect formation mechanism and suppression strategy in additively manufactured tungsten grid

thin-wall structures via laser powder bed fusion. *J. Manuf. Process.* **120**, 222–233.
[32] Wang M et al. 2024. Molten pool behaviors and printability of tungsten anti-scattering grids with extremely thin wall thickness fabricated via laser powder bed fusion. *Addit. Manuf.* **94**, 104487.
[33] Ding J H, Qu S, Zhang L, Wang M Y and Song X. 2022. Geometric deviation and compensation for thin-walled shell lattice structures fabricated by high precision laser powder bed fusion. *Addit. Manuf.* **58**, 103061.
[34] Zhang L, Lifton J, Hu Z H, Hong R C and Feih S. 2022. Influence of geometric defects on the compression behaviour of thin shell lattices fabricated by micro laser powder bed fusion. *Addit. Manuf.* **58**, 103038.
[35] Tan S J, Zhang X, Wang Z Y, Ding L P, Chen W L and Zhang Y C. 2022. Characterization of triply periodic minimal surface structures obtained using toolpath-based construction design. *Mater. Sci. Addit. Manuf.* **1**, 17.
[36] Jia H L, Sun H, Wang H Z, Wu Y and Wang H W. 2021. Scanning strategy in selective laser melting (SLM): a review. *Int. J. Adv. Manuf. Technol.* **113**, 2413–2435.
[37] Wu Y H, Gupta A, Kurzeja K and Rossignac J. 2020. ChoCC: convex hull of cospherical circles and applications to lattices. *Comput. Aided Des.* **129**, 102903.
[38] Minetto R, Volpato N, Stolfi J, Gregori R M M H and da Silva M V G. 2017. An optimal algorithm for 3D triangle mesh slicing. *Comput. Aided Des.* **92**, 1–10.
[39] Bhandari S. 2022. A graph-based algorithm for slicing unstructured mesh files. *Addit. Manuf. Lett.* **3**, 100056.
[40] Wu Y, Chen X S, Sun R J, He C Q, Hu J L and Han S Z. 2024. Research on adaptive slicing method for optimizing STL model manufacturing details. *Int. J. Adv. Manuf. Technol.* **130**, 4459–4468.
[41] Ding J H, Zou Q, Qu S, Bartolo P, Song X and Wang C C L. 2021. STL-free design and manufacturing paradigm for high-precision powder bed fusion. *CIRP Ann.* **70**, 167–170.
[42] Wang S L, Zhang L-C, Cai C, Tang M-K, Chen S, Huang J and Shi Y-S. 2024. Universal and efficient hybrid modeling and direct slicing method for additive manufacturing processes. *Adv. Manuf.* **12**, 300–316.
[43] Feng J W, Fu J Z, Lin Z W, Shang C and Niu X M. 2019. Layered infill area generation from triply periodic minimal surfaces for additive manufacturing. *Comput. Aided Des.* **107**, 50–63.
[44] Zhang L, Hu Z H, Wang M Y and Feih S. 2021. Hierarchical sheet triply periodic minimal surface lattices: design, geometric and mechanical performance. *Mater. Des.* **209**, 109931.
[45] Isaac C W and Duddeck F. 2022. Current trends in additively manufactured (3D printed) energy absorbing structures for crashworthiness application–a review. *Virtual Phys. Prototype* **17**, 1058–1101.
[46] Toby B H. 2001. *EXPGUI*, a graphical user interface for *GSAS*. *J. Appl. Cryst.* **34**, 210–213.
[47] Lim Y and Ha S. 2023. RufGen: a plug-in for rough surface generation in Abaqus/CAE. *SoftwareX* **22**, 101380.
[48] Demir E, Martinez-Pechero A, Hardie C and Tarleton E. 2025. OXFORD-UMAT: an efficient and versatile crystal plasticity framework. *Int. J. Solids Struct.* **307**, 113110.
[49] Depriester D and Kubler R. 2020. MTEX2Gmsh: a tool for generating 2D meshes from EBSD data. *J. Open Source Softw.* **5**, 2094.
[50] Chen H, Wei Q S, Zhang Y J, Chen F, Shi Y S and Yan W T. 2019. Powder-spreading mechanisms in powder-bed-based additive manufacturing: experiments and computational modeling. *Acta Mater.* **179**, 158–171.
[51] Körner C, Bauereiß A and Attar E. 2013. Fundamental consolidation mechanisms during selective beam melting of powders. *Modelling Simul. Mater. Sci. Eng.* **21**, 085011.
[52] Masmoudi A, Bolot R and Coddet C. 2015. Investigation of the laser–powder–atmosphere interaction zone during the selective laser melting process. *J. Mater. Process. Technol.* **225**, 122–132.
[53] Yoo D J. 2014. Advanced projection image generation algorithm for fabrication of a tissue scaffold using volumetric distance field. *Int. J. Precis. Eng. Manuf.* **15**, 2117–2126.
[54] de Leon Nope G V, Perez-Andrade L I, Corona-Castuera J, Espinosa-Arbelaez D G, Muñoz-Saldaña J and Alvarado-Orozco J M. 2021. Study of volumetric energy density limitations on the IN718 mesostructure and microstructure in laser powder bed fusion process. *J. Manuf. Process.* **64**, 1261–1272.
[55] Ma K K, Wen H, Hu T, Topping T D, Isheim D, Seidman D N, Lavernia E J and Schoenung J M. 2014. Mechanical behavior and strengthening mechanisms in ultrafine grain precipitation-strengthened aluminum alloy. *Acta Mater.* **62**, 141–155.
[56] Smith T R, Sugar J D, San Marchi C and Schoenung J M. 2019. Strengthening mechanisms in directed energy deposited austenitic stainless steel. *Acta Mater.* **164**, 728–740.
[57] Feng Z Y, Li H, Zhang D, Guo X X, Chen Y Q and Fu M W. 2022. Multi-aspect size effect transition from micro to macroscale: modelling and experiment. *Int. J. Plast.* **156**, 103364.
[58] Dong Z, Han C, Zhao Y, Huang J, Ling C, Hu G, Wang Y, Wang D, Song C and Yang Y. 2024. Role of heterogenous microstructure and deformation behavior in achieving superior strength-ductility synergy in zinc fabricated via laser powder bed fusion. *Int. J. Extrem. Manuf.* **6**, 045003.
[59] Kolken H M A, Garcia A F, Plessis A D, Meynen A, Rans C, Scheys L, Mirzaali M J and Zadpoor A A. 2022. Mechanisms of fatigue crack initiation and propagation in auxetic metabiomaterials. *Acta Biomater.* **138**, 398–409.
[60] Yang L, Yan C Z, Cao W C, Liu Z F, Song B, Wen S F, Zhang C, Shi Y S and Yang S F. 2019. Compression–compression fatigue behaviour of gyroid-type triply periodic minimal surface porous structures fabricated by selective laser melting. *Acta Mater.* **181**, 49–66.
[61] Gibson L J and Ashby M F. 1997. *Cellular Solids: Structure and Properties* 2nd edn (Cambridge University Press, Cambridge).
[62] Wang Y J, Zhang X, Li Z H, Gao H J and Li X Y. 2022. Achieving the theoretical limit of strength in shell-based carbon nanolattices. *Proc. Natl Acad. Sci. USA* **119**, e2119536119.
[63] Fu J, Qu S, Ding J H, Song X and Fu M W 2021. Effect of heat treatment on microstructures and mechanical properties of SS316L by micro selective laser melting. *In Proceedings of the 16th International Manufacturing Science and Engineering Conference* (American Society of Mechanical Engineers, New York) p V001T001A005.
[64] Li W Q, Meng L X, Niu X F and Zhou W. 2024. Microstructure, mechanical properties, and deformation behaviour of LPBF 316L via post-heat treatment. *Virtual Phys. Prototype* **19**, e2405623.
[65] Li W B, Ding J H, Chen X, Wang Y, Song X and Zhang S. 2024. A 3D-printed CuNi alloy catalyst with a triply periodic minimal surface for the reverse water-gas shift reaction. *J. Mater. Chem. A* **12**, 314–320.
[66] Zhang T, Liu F, Zhang K F, Zhao M, Zhou H L and Zhang D Z. 2023. Numerical study on the anisotropy

in thermo-fluid behavior of triply periodic minimal surfaces (TPMS). *Int. J. Heat Mass Transfer* **215**, 124541.

[67] Baobaid N, Ali M I, Khan K A and Al-Rub R K A. 2022. Fluid flow and heat transfer of porous TPMS architected heat sinks in free convection environment. *Case Stud. Therm. Eng.* **33**, 101944.

[68] Kadivar M, Tormey D and McGranaghan G. 2024. CFD of roughness effects on laminar heat transfer applied to additive manufactured minichannels. *Heat Mass Transfer* **60**, 1915–1929.

[69] Ma R, Alamé K and Mahesh K. 2021. Direct numerical simulation of turbulent channel flow over random rough surfaces. *J. Fluid Mech.* **908**, A40.